International Journal of Biological Macromolecules 272 (2024) 132589

Contents lists available at ScienceDirect

International Journal of Biological Macromolecules

journal homepage: www.elsevier.com/locate/ijbiomac

Edge-functionalized coal-derived graphene oxide in bacterial nanocellulose hydrogel for active wound healing

Chithra Lekha P [a,h,*], Marini L [b], Suman K. Jhajharia [a,c], Aadinath W [d], Vignesh Muthuvijayan [d], Mareeswari Paramasivan [a], Monica Chingchuilin Gonmei [a], M.K. Padmanabhan [e], Madhan Jeyaraman [f], Roop L. Mahajan [g,**]

[a] Centre for Clinical and Translational Research, Healthcare Technologies Division, Virginia Tech India Research and Education Forum, Indian Institute of Technology Madras Research Park, Chennai 600 113, Tamil Nadu, INDIA
[b] Centre for Nanoscience and Technology, AC Tech Campus, Anna University, Chennai 600 025, Tamil Nadu, India
[c] Department of Mechanical Engineering, Virginia Tech, Blacksburg, VA 24061, USA
[d] Department of Biotechnology, Bhupat and Jyoti Mehta School of Biosciences, Indian Institute of Technology Madras, Chennai 600 036, Tamil Nadu, INDIA
[e] Dr MGR Educational and Research Institute, Chennai, Tamil Nadu 600 095, INDIA
[f] Department of Orthopaedics, ACS Medical College and Hospital, Dr MGR Educational and Research Institute, Chennai, Tamil Nadu 600 077, INDIA
[g] Department of Mechanical Engineering, Department of Materials Science and Engineering, Virginia Tech, Blacksburg, VA 24061, USA
[h] Department of Physics, Dr MGR Educational and Research Institute, Madhuravoyal, Chennai 600 095, Tamil Nadu, INDIA

ARTICLE INFO

Keywords:
Bacterial Nanocellulose
Hydrogel
Coal-derived graphene oxide
Face-to-edge assembly
Active wound dressing

ABSTRACT

This work presents a comparison of physicochemical and *in vitro* active wound healing properties of two distinct Graphene Oxides (GOs) from graphite and coal. These GOs are incorporated in Bacterial Nanocellulose (BNC) to form hydrogels. The performance and limitations of the loading fraction of both GOs in BNC are controlled by the processing technology and the source materials from which GOs are derived. Edge functionalization with C-GO offers the advantage of facilitating face-to-edge assembly in the hydrogel leading to better dispersion than the face-to-face assembly of basal functionalized G-GO. The latter leads to more aggregation of G-GO, resulting in a lower optimal loading fraction. Our investigation into the antibacterial properties of the BNC and BNC/GO hydrogels against gram-negative *E. coli* revealed inhibitory effects of the BNC/GO hydrogels that intensified with an increase in the concentration of GO. Furthermore, an *in vitro* wound scratch assay demonstrated that BNC/C-GO hydrogels promote better cell migration, confirming their superior biocompatibility and suitability as active wound dressings, albeit limited by loading fraction due to agglomeration. These findings shed light on the performance and limitations of GOs for diverse applications, emphasizing the significance of exploring the influence of different methods and source materials of GOs.

1. Introduction

The skin, an enormous organ of the human body, plays a vital role as an interface between the body and its surroundings. It serves as a barrier against water loss and blocks microbial invasion [1–3]. Loss of skin integrity because of injury can lead to major disabilities or can even be fatal [4]. These injuries commonly occur as a result of mechanical, thermal, and chemical actions, as well as various chronic pathophysiological conditions [3]. Although the skin has inherent mechanisms for self-repair and restoration of its structural features and functional stability, effective and reliable wound care intervention and management are crucial to prevent desiccation and further infection of open wounds, accelerate the healing process, reduce pain, and minimize scar formation [2].

Wound healing is a complex and dynamic process that initiates shortly after the formation of a wound and aims to restore and reconstruct the integrity of the skin. It involves four major processes: hemostasis, inflammation, cellular proliferation, and remodeling of the Extracellular Matrix (ECM) [5,6]. Traditional methods of wound treatment often involve the use of dry gauzes and bandages, which fail to

* Correspondence to: C.L. P, Centre for Clinical and Translational Research, Healthcare Technologies Division, Virginia Tech India Research and Education Forum, Indian Institute of Technology Madras Research Park, Chennai 600 113, Tamil Nadu, INDIA.
** Corresponding author.
E-mail addresses: drlekhapc@gmail.com (C.L. P), mahajanr@vt.edu (R.L. Mahajan).

https://doi.org/10.1016/j.ijbiomac.2024.132589
Received 30 August 2023; Received in revised form 10 May 2024; Accepted 21 May 2024
Available online 22 May 2024
0141-8130/© 2024 Elsevier B.V. All rights are reserved, including those for text and data mining, AI training, and similar technologies.

create a moist environment, thereby making the wound vulnerable to infections and trauma upon their removal [7–9]. To overcome these shortcomings, the development of active wound dressing materials has an important role to play in promoting effective wound healing [8].

Various currently developed functional wound dressings such as nanofibers, hydrocolloids, foams, and hydrogels exhibit distinct therapeutic effects on wound healing [5]. Among these, hydrogels, which are essentially polymeric networks that have hydrophilic properties, have emerged as novel biomaterials that mimic the 3D ECM of the skin. They possess efficient oxygen permeability, maintain a moist environment at the wound interface, promote rapid wound healing, and are gentle upon removal [8]. Among the polymers, natural polymers are preferred over synthetic polymers due to their cost-effectiveness and biocompatibility [8,10]. One such natural polymer is biopolymer BNC, which is synthesized through a green process involving bacteria. It exhibits excellent biocompatibility, biodegradability, and purity, characterized by its ultra-fine network structure and many desirable physicochemical features such as tensile strength, crystallinity, and absorption capacity. These qualities position BNC as a promising biomaterial for wound dressings and scaffolds [8,11–13]. Moreover, BNC exhibits high stability, low toxicity, and non-allergenic properties, making it safe for sterilization. Although BNC alone lacks antibacterial properties, its application is limited to passive wound dressing. However, when combined with antibacterial materials to form composites, BNC can serve as a key material for active wound dresser [14].

With the advancement of nanotechnology, GO has attracted significant interest in biomedical applications [15,16]. As, a carbonaceous 2D nanomaterial, it is a chemically functionalized derivative of graphene that has excellent mechanical strength, thermal conductivity, large surface area, high adsorption capability, biocompatibility, biodegradability, accelerated cellular adhesion, proliferation, and differentiation [17,18]. Not surprisingly, it has been extensively studied in various applications such as a scaffold material in tissue regeneration, gene therapy, photothermal treatment, biotechnology techniques such as proteomics, adsorption, and as an antibacterial [19,20]. Various GO-polymer scaffolds, nanocomposites, and hydrogels have been investigated for wound healing. These include, among others, GO-cellulose nanocomposite [19], Glycidyl methacrylate functionalized Quaternized Chitosan (QCSG)/Gelatin Methacrylate (GM)/GO hydrogels [21], O-Carboxymethyl Chitosan (CS)/Poly Vinyl Alcohol (PVA), GO double network hydrogel [22], nanocomposite polyurethane/polycaprolactone scaffolds with GO [23], GO/Gelatine (Gel)/Trypsin (Try) hydrogel for the electro-responsive release of Curcumin (Cur) [24], PVA/GO nanofibrous scaffolds [25], 3D Hydroxyapatite (HA)/GO/CS ternary composite hydrogels [26], CS/bacterial cellulose nanofibrous composites [27], GO-Regenerated Cellulose (RCE)/PVA ternary hydrogels [28], PVA/CS/GO nanofibers [29], Ag/graphene polymer hydrogel [30], Reduced Graphene Oxide (rGO)-enriched CS hydrogel/cellulose acetate-based nanofibers [31], PVA/*Moringa oleifera*/GO [32], GO functionalized bacterial cellulose-gelatin hydrogel [33], GO-based injectable conductive hydrogel dressing [34], and arabinoxylan functionalized-GO based composite hydrogel for skin tissue engineering [35].

Recently, coal—an inexpensive and abundantly available natural resource—has emerged as a precursor for synthesizing graphene oxide (C-GO) using a facile one-pot method. This method offers a more economical and environmentally friendly alternative to the traditional modified Hummers' method, which utilizes graphite to produce graphene oxide (G-GO) [36,37]. Notably, these two different methods lead to two chemically distinct graphene oxide structures—edge-functionalized C-GO and basal-functionalized G-GO [36,38].

In this study, we have synthesized and evaluated a BNC hydrogel incorporated with C-GO as an antimicrobial wound dressing material and compared its performance with that of G-GO. Our hypothesis was that compared to G-GO, C-GO with its abundant edge carboxylic groups, would exhibit improved dispersion [39], which, in turn, would result in superior wound dressing and enhanced antibacterial activity. Mindful of the accessiblility of raw materials and cost-efficiency, we employed an innovative and cost-effective freeze-thaw method to synthesize the hydrogels by incorporating different weight percentages of both G-GO and C-GO onto the BNC surfaces. We obtained and characterized a series of hydrogels with varying morphology and physicochemical properties. Subsequently, we conducted *in vitro* cytotoxicity wound scratch assays and antibacterial studies to assess the influence of C-GO and G-GO weight percentages on the relative performance of the synthesized hydrogels. As discussed in detail in the forthcoming sections, our findings support the superiority of BNC/C-GO hydrogels over their G-GO counterparts as an optimal active wound dressing material.

2. Materials and methods

2.1. Materials

BNC was cultivated from a kombucha tea culture. Commercial-grade sodium hydroxide (NaOH) pellets and urea were purchased from Merck. Graphite (200 μm) was purchased from Sigma Aldrich. Epichlorohydrin (99%) was obtained from Sisco Research Laboratories Pvt. Ltd., and anthracite coal was received from SV Ispat Pvt. Ltd. India, having 88% to 90% of fixed carbon, 4% of volatile matter, 7% to 8% of ash, and 5% of moisture content. All chemicals other than coal were used as received without further purification.

2.2. Synthesis of BNC and GO

We synthesized BNC in our laboratory using a kombucha culture grown at room temperature. The culture was prepared following the standard recipe as reported elsewhere [40]. After 7 days the newly formed kombucha cellulose with a thickness of 2-5 mm was collected. The cellulose was washed with water to remove the yeast residues and treated with 2% NaOH while maintaining a neutral pH. GO was prepared from coal and natural graphite using the facile one-pot method [36] and the modified Hummers' method [41], respectively.

2.3. Preparation of BNC/GO hydrogels

For the GO dispersion, a measured quantity of GO was added to 30 mL of deionized water and the bath was ultra-sonicated for 2 h at a temperature below 40°C. Then, 30 g of BNC was added to the dispersed GO and stirred for 15 min at 500 rpm. An aqueous solution of 14 wt% of NaOH and 7 wt% of urea in deionized water was prepared to dissolve the BNC/GO composite. The BNC/GO suspension was added to the solution, stirred for 5 min, and placed in a freezer at −20 °C for 12 h. The frozen semi-solid solution was thawed for two cycles, resulting in a transparent BNC/GO solution. Epichlorohydrin was added as a cross-linking agent to the BNC/GO solution which was stored at −20 °C for 12 h. The resulting hydrogels were centrifuged, washed several times with deionized water to neutral pH, and then lyophilized. BNC hydrogel was also prepared with the same composition but without adding GO. A series of BNC/GO hydrogels were prepared with different weight percentages of GO (0.01 wt%, 0.05 wt%, and 0.10 wt%). Throughout the experiment, G-GO was used to compare the functional properties of C-GO in every aspect. The resultant BNC/GO hydrogels were labelled G-GO1, G-GO5, G-GO10 for graphite-derived GO, and C-GO1, C-GO5, and C-GO10 for the coal-derived GO, respectively.

2.4. Physicochemical characterizations

To analyze the particle size distribution of BNC, G-GO, and C-GO, a laser scattering particle size distribution analyzer LA-950 (HORIBA) was used. The calculations for particle size distribution were performed on a volume basis. Particle size distribution of BNC hydrogel, G-GO5, and C-GO5 were evaluated using Dynamic Light Scattering (DLS) Microtrac. The morphology of the as-prepared BNC hydrogel and BNC/GO

hydrogels was observed using SEM (VEGA3 TESCAN) at an accelerating voltage of 30 kV and TEM (JEOL Japan, JEM-2100 Plus). For SEM observation, the lyophilized hydrogel samples were coated with a thin layer of gold. TEM provided data for Selected Area Electron Diffraction (SAED) and Energy Dispersive X-ray Analysis (EDAX) for the lyophilized hydrogel samples. The structure and composition of functional groups G-GO, C-GO, BNC, BNC hydrogel, and BNC/GO hydrogels were analyzed using an FT-IR spectrometer (Bruker Alpha). Spectra were recorded with a resolution of 1 cm^{-1}, covering the wavenumber range of 4000–500 cm^{-1}. XRD patterns were obtained using a Powder X-ray Diffractometer D8 advance (Bruker) in reflection mode, using samples of the lyophilized hydrogel samples without milling, using the wavelength of monochromatic Cu-Kα radiation (wavelength 1.5406 Å) at an operating current of 30 mA and voltage of 40 kV. The patterns were recorded over the 2θ range of 5°–80°. To investigate the thermal properties of the hydrogels, TG-DTA was carried out using an SDT Q600 V20.9 Build 20 TA Instrument. The lyophilized samples were placed in the TGA furnace and measurements were carried out under an argon atmosphere, using a heating rate of 10°C/min from 25°C to 600°C.

The porosity of the hydrogel was assessed using the liquid displacement technique [42]. Hydrogels were taken at known volume of size 1 cm *1 cm. These prepared hydrogels were immersed in ethanol and placed in vacuum environment for 1 h. The initial weight (Wi) prior to immersion and the final weight (Wf) following immersion in ethanol were noted. The porosity (%) was calculated using the formula

$$\in \left(\%\right) = \frac{Wf - Wi}{\rho V}$$

where ρ is the density of ethanol.

For the swelling studies, the hydrogel was cut into small sections, weighed (Wi), and studied for its swelling ability using Phosphate Buffered Saline (PBS) absorption assay [42]. The weighted scaffolds were submerged in PBS (pH 7.4) for 60 min at 37°C. The inflated scaffolds were removed and absorbed water molecules were removed using filter paper and weighed immediately (Wf). The weight of the absorbed PBS to the initial dry weight of the scaffold was used to calculate the degree of swelling.

$$\%\text{Swelling} = \frac{(Wf - Wi)}{Wi} * 100$$

PBS was used to investigate the hydrogel's *in vitro* degrading characteristics [43]. The materials were weighed in triplicate before being submerged in PBS containing 1% lysozyme in a 15 mL plastic tube. For 28 days, the tubes were shaken on an orbital shaker at 37°C. After a specific period, the samples were removed, cleaned with deionized water, and dried in a hot air oven at 60°C. The weight loss of the samples from their initial dry weight was used to calculate their degradation. The degradation behavior of the samples during PBS immersion was estimated from the original dry weight, and this method was repeated for a total of 28 days. The degradation rate was calculated as

$$\%\text{degradation} = \frac{(Wi - Wf)}{Wi} * 100$$

where Wi and Wf are the initial and final weight of hydrogel before and after immersion in PBS respectively.

2.5. In vitro studies

2.5.1. Cytotoxicity assay

The biocompatibility of the hydrogels was assessed using an Alamar blue assay through cell viability of L929 fibroblast cell lines. The L929 cells were seeded in 96 well plates for cell cytotoxicity studies employing the Alamar blue assay. Once a monolayer was formed, the hydrogels were removed by cutting. After 24 h, the samples were dislodged from the wells and the wells were thoroughly washed to remove the cells present. Alamar blue (0.1 mg/mL) was added to each well and incubated for 2 h in a 5% CO_2 atmosphere at 37°C. Optical Density (OD) measurements were taken at 570 and 600 nm, and cell viability was calculated by comparing the OD values with those of the control (Tissue Culture Plate, TCP).

$$\textit{Cell viability}\% = \frac{(O_2 \times A_{570} - O_1 \times A_{600})}{(O_2 \times C_{570} - O_1 \times C_{600})} \times 100\%$$

where, A_{570} and A_{600} are the absorbance values of the hydrogels well at 570 nm and 600 nm, respectively, and C_{570} and C_{600} are the absorbance values of the control wells at 570 nm and 600 nm, respectively. The optical absorption coefficients of the dye in reduced and oxidized form, O_1, and O_2, are 80,586 and 117,256, respectively. The methodology adhered to standard guidelines.

2.5.2. Antibacterial efficiency of BNC hydrogel and BNC/GO hydrogels

The antibacterial activities of BNC and BNC/GO hydrogels were evaluated using the well-diffusion method against gram-negative bacteria *E. coli*. Mueller–Hinton Broth (MHB) was prepared and the target *E. coli* strain was cultured in the medium for 24 h. The resulting suspension was appropriately diluted to maintain a standard subculture. Mueller Hinton Agar (MHA) was prepared and poured into a sterile petri dish, allowing the medium to solidify. The freshly prepared *E. coli* pathogens were inoculated onto the solidified MHA. Agar well discs, 6 mm in diameter were created using a sterile cork borer. To assess the sensitivity of each hydrogel sample with microbial properties, the standard drug gentamicin (20 μg) was used as the positive control. Different concentrations of hydrogel samples (10, 20, 40, and 80 μg/mL) were loaded into separate agar wells. The seeded petri dishes containing the hydrogel samples were then incubated at 37°C for 24 h. Subsequently, the diameter of the distinct Zone of Inhibition (ZOI) surrounding each agar well disc was measured to determine the antibacterial activity of the hydrogel against the bacteria.

2.5.3. Wound scratch assay

The *in vitro* wound scratch assay is a widely used and cost-effective method to measure cell migration *in vitro,* providing a potential mimicry *in vivo* cell migration to a certain extent [44]. It is also an essential standard process for evaluating the wound-healing properties of novel wound treatment products [45]. To evaluate the efficacy of the hydrogels as wound-healing materials, 3T3 fibroblast cells were cultured in 6-well plates at a density of 8×10^5 cells/well under optimal culture conditions. Once the cells reached their optimal growth phase, a wound was created by manually scratching the cell monolayer using a sterilized P10 pipette tip. Subsequently the detached cells were washed off with a fresh medium. The created wounds were then treated with 50 μg/mL of G-GO5 and C-GO5 treated media and incubated for 3 days at 37°C to evaluate healing capacity. The percentage of wound healing for the control, G-GO5, and C-GO5 was determined by evaluating the extent of cell migration indicated by the closure of the scratch after each day of the wound introduction [46]. For better visualization of cell migration after creating scratch, cells were stained with acridine orange dye before capturing the images under microscope. Briefly, after a certain time point, treated hydrogels and media were removed from the wells and washed multiple times with PBS. To each well, 1 mL of acridine orange solution (100 μg/mL) was added and left for 10 min at room temperature. Then images were captured under fluorescence microscope.

3. Results and discussion

3.1. Size distribution and morphology

The particle size measurements presented in Fig. 1 reveal that the mean size of the particle distribution for pristine BNC, G-GO, and C-GO are 541 μm, 23 μm, and 0.7 μm, respectively. Notably, the G-GO

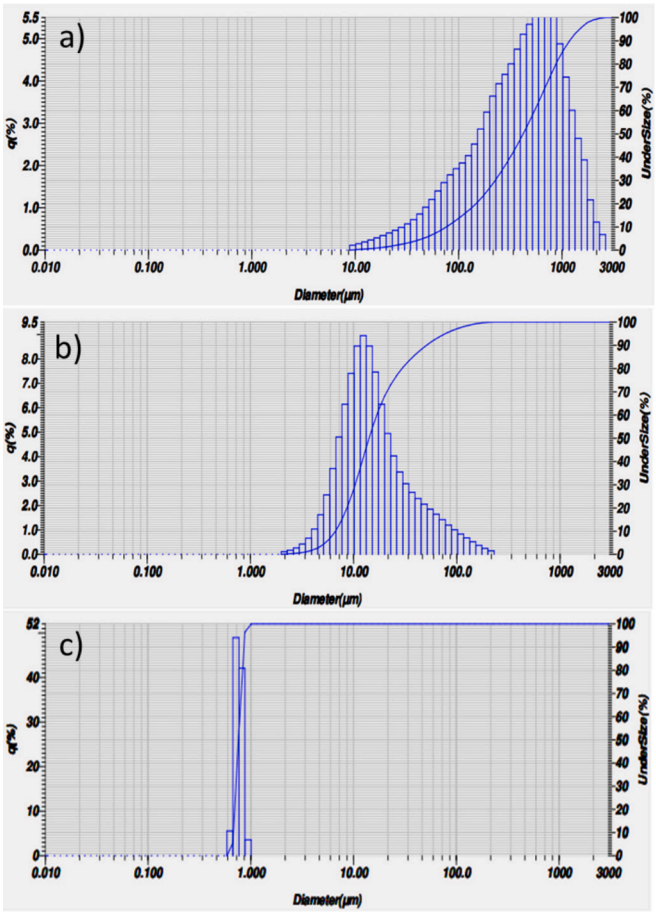


Fig. 1. Particle size distribution of pristine a) BNC, b) G-GO, and c) C-GO.

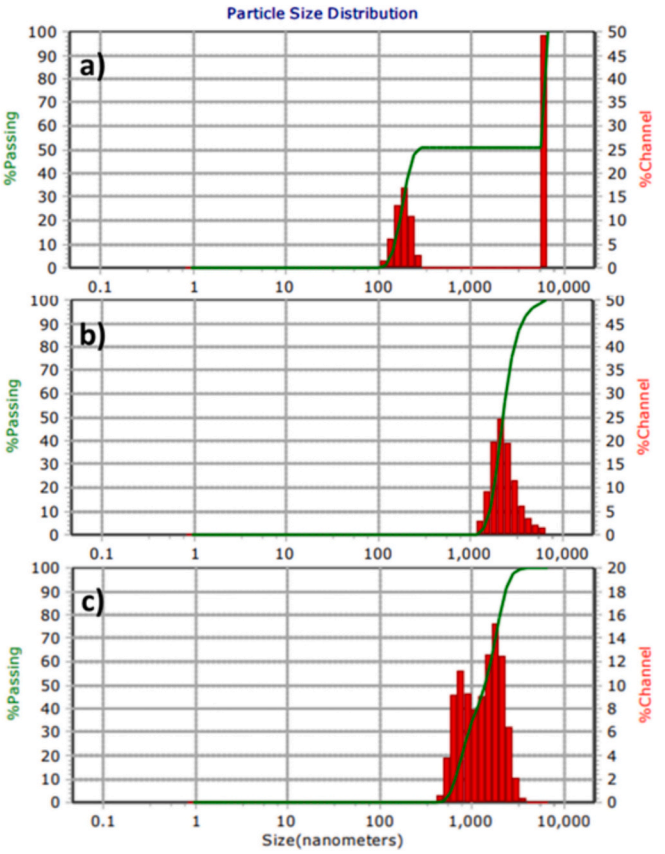


Fig. 2. DLS of hydrogels a) BNC, b) G-GO5, and c) C-GO5.

suspension contains sheets with larger lateral sizes [47], resulting in a higher mean size of particles, which can lead to agglomeration at higher loading fractions. On the other hand, C-GO exhibits a narrow size distribution compared to G-GO, with a mean measured diameter of approximately 0.7 μm. This narrow size distribution is advantageous as it enables C-GO to disperse uniformly within the BNC hydrogel network.

The particle size distribution of BNC hydrogel, G-GO5, and C-GO5, as depicted in Fig. 2, reveals mean diameter intensity distribution of 3.1 μm, 2.4 μm, and 1.4 μm respectively. The formation of a hydrogel matrix results in reduction of the particle size in comparison to the raw materials. The polydispersity index is 0.68, 0.08, and 0.24 for BNC hydrogel, G-GO5, and C-GO5 respectively. Notably G-GO5 shows a narrow size distribution with suspended particles while C-GO5 implies highly dispersed pore size distribution.

The morphology of the fibrous BNC hydrogel, along with the incorporation of planar GO, was confirmed by the SEM and TEM images. As the concentration of GO incorporated into BNC hydrogels increased, a more pronounced network structure of hydrogel along with the planar morphology of GO was observed, as depicted in Fig. 3. The 3D network of hydrogel intercalated with 2D platelets of GO resulted in the formation of large pores and high surface area, indicating good interaction between the composite phases. Fig. 3b shows G-GO1 to exhibit a closely packed network structure compared to that of C-GO. With a further increase in the loading fraction to 0.05 wt%, agglomeration of hydrogels started in G-GO (Fig. 3c), while well-defined pores were observed in C-GO5 (Fig. 3f). G-GO10 revealed complete agglomeration, whereas, in C-GO10, agglomeration had just begun. The implication is that the onset of agglomeration takes place in C-GO at a higher loading fraction as compared to that of G-GO. This, as will be discussed later, has implications on the performance of the hydrogel for wound dressing.

The TEM image in Fig. 4 provides insight into morphology of BNC hydrogel, G-GO5, and C-GO5 revealing the characteristics of the GO incorporated into the hydrogel network. BNC hydrogel displays a larger pore size distribution, but upon the introduction of GO a more even surface morphology was observed as indicated in the SEM image. C-GO5 shows a notably even surface morphology in comparison to G-GO5, which can be attributed to the smaller size of particle distribution and face-to-edge assembly demonstrating better dispersion of GO [48]. The EDAX confirms the element composition of BNC hydrogel and GO hydrogels. As shown in Fig. 5 the BNC hydrogel consists of 76 wt% of carbon and 24 wt% of oxygen group while G-GO5 and C-GO5 were 83 wt %,47 wt% of carbon and 17 wt%, 53 wt% of oxygen, respectively. The abundance of oxygen group in C-GO5 supports the face-to-edge assembly with BNC as discussed in the following section.

3.2. *Structural characterization of BNC hydrogel and BNC/GO hydrogels*

The FT-IR technique was employed to identify different functional groups present in the hydrogel samples and investigate possible bonding during the networking process. Focusing on the spectra patterns for G-GO and C-GO in Fig. 6, we note the presence of various types of oxygen functional groups. The FT-IR spectra reveal that the peak at ~3100 cm^{-1} corresponding to the -OH functional groups, and another peak at ~1060 cm^{-1} attributable to epoxy groups are stronger in G-GO compared to those in C-GO. On the other hand, the peak at ~1715 cm^{-1} related to -COOH groups is more intense in C-GO as compared to that in G-GO. Furthermore, a broad peak in the region 3300–2500 cm^{-1} was observed in the spectrum for C-GO, which is mainly attributed to the -O–H stretch of carboxylic acid, along with hydroxylic groups centered at about 3100 cm^{-1}. We further note that the -OH and epoxy groups are predominantly present on basal planes of GO, whereas the -COOH groups are primarily located on the edges of the graphitic planes. These results illustrate the

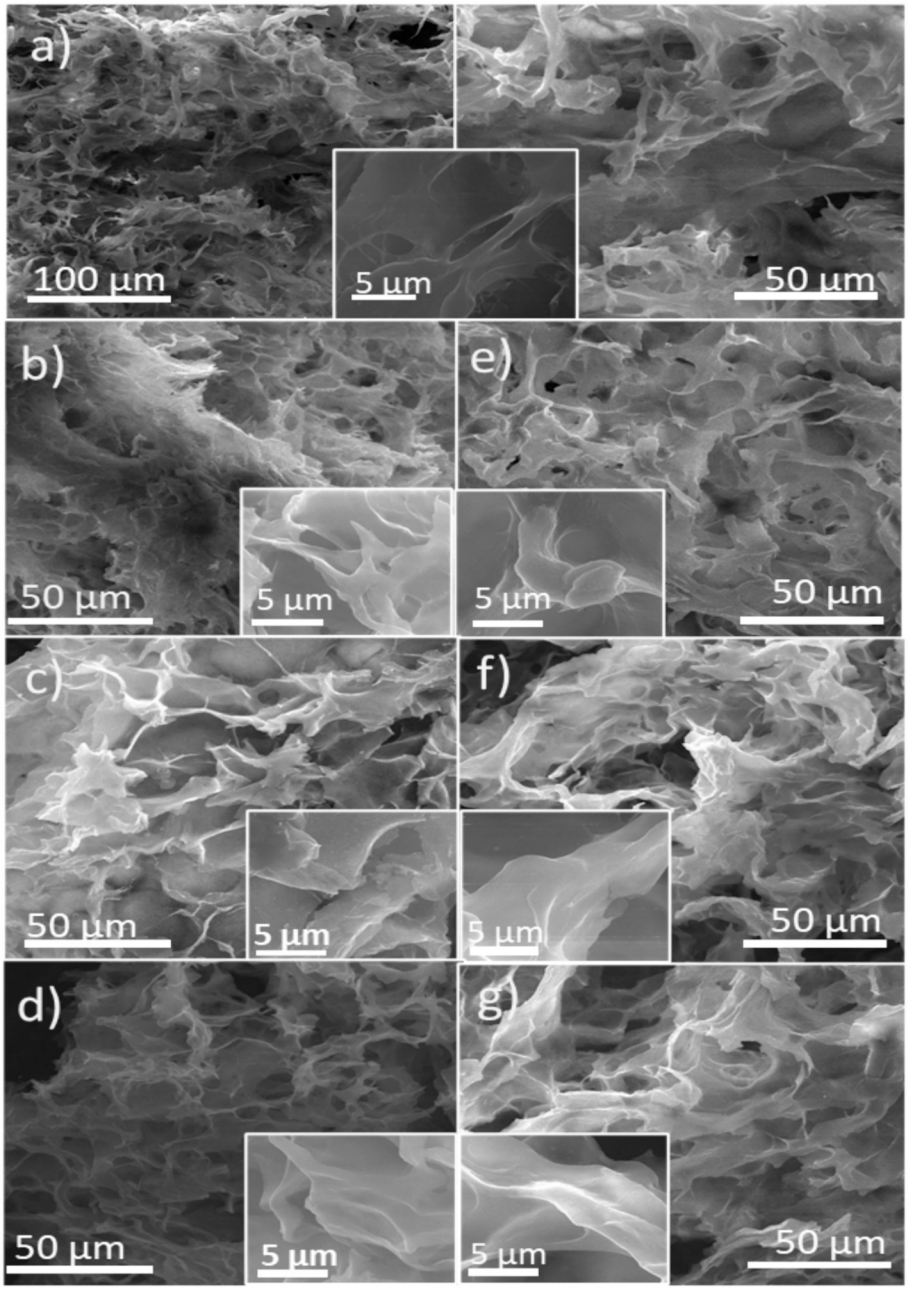


Fig. 3. SEM image of a) BNC hydrogel, b) G-GO1, c) G-GO5, d) G-GO10, e) C-GO1, f) C-GO5, and g) C-GO10.

distinct chemical nature of G-GO and C-GO; the former has a dominance of the basal oxygen functional groups while the latter is dominated by the edge functional groups.

The FT-IR spectrum of BNC (Fig. 6b) shows mainly -OH group stretching and bending peaks corresponding to the presence of abundant hydroxyl groups on the cellulose backbone. During the formation of the BNC hydrogel where epichlorohydrin works as a linker, the two -OH groups of BNC form two epoxy groups and an -OH group (Scheme 1) resulting in a decrease in intensity of -OH groups accompanied by the appearance of a new epoxy peak at ~1026 cm^{-1} as shown in Fig. 6 & Scheme 1. A successful formation of the BNC hydrogel is confirmed. The FT-IR spectra of the BNC hydrogel, BNC/C-GO, and BNC/G-GO hydrogels are compared in Fig. 7a. It is evident that the dominant BNC hydrogel peaks are present in BNC/GO hydrogels proving the retention of network structure during the incorporation of GO.

As we discussed earlier, G-GO has an abundance of basal functional groups, whereas C-GO has a dominance of edge functional groups. This difference in functionalization leads to distinct modes of interaction with BNC. G-GO primarily engages in face-to-face assembly with BNC, while C-GO undergoes face-to-edge assembly with BNC, as illustrated in Scheme 1. The evidence of this assembly is supported by the presence of peaks at 1730 cm^{-1}, 1453 cm^{-1} related to ester group in Fig. 7a. These peaks are more intense in BNC/C-GO hydrogel as compared to BNC/G-GO hydrogel. The assignment of functional groups for BNC, G-GO, C-GO, and the hydrogels are shown in Table 1.

The crystallographic structure of various BNC/GO hydrogels were analyzed and compared with that of BNC hydrogel, C-GO, and G-GO. Fig. 7b shows the XRD profiles of G-GO, C-GO, BNC hydrogel, and BNC/GO hydrogels G-GO1, G-GO5, G-GO10, C-GO1, C-GO5, and C-GO10. G-GO shows a distinct diffraction peak of C (001) at 2θ equal to 11° [49], signifying successful exfoliation of graphite and the intercalation of oxygen functional groups. C-GO, on the other hand, shows a distinct

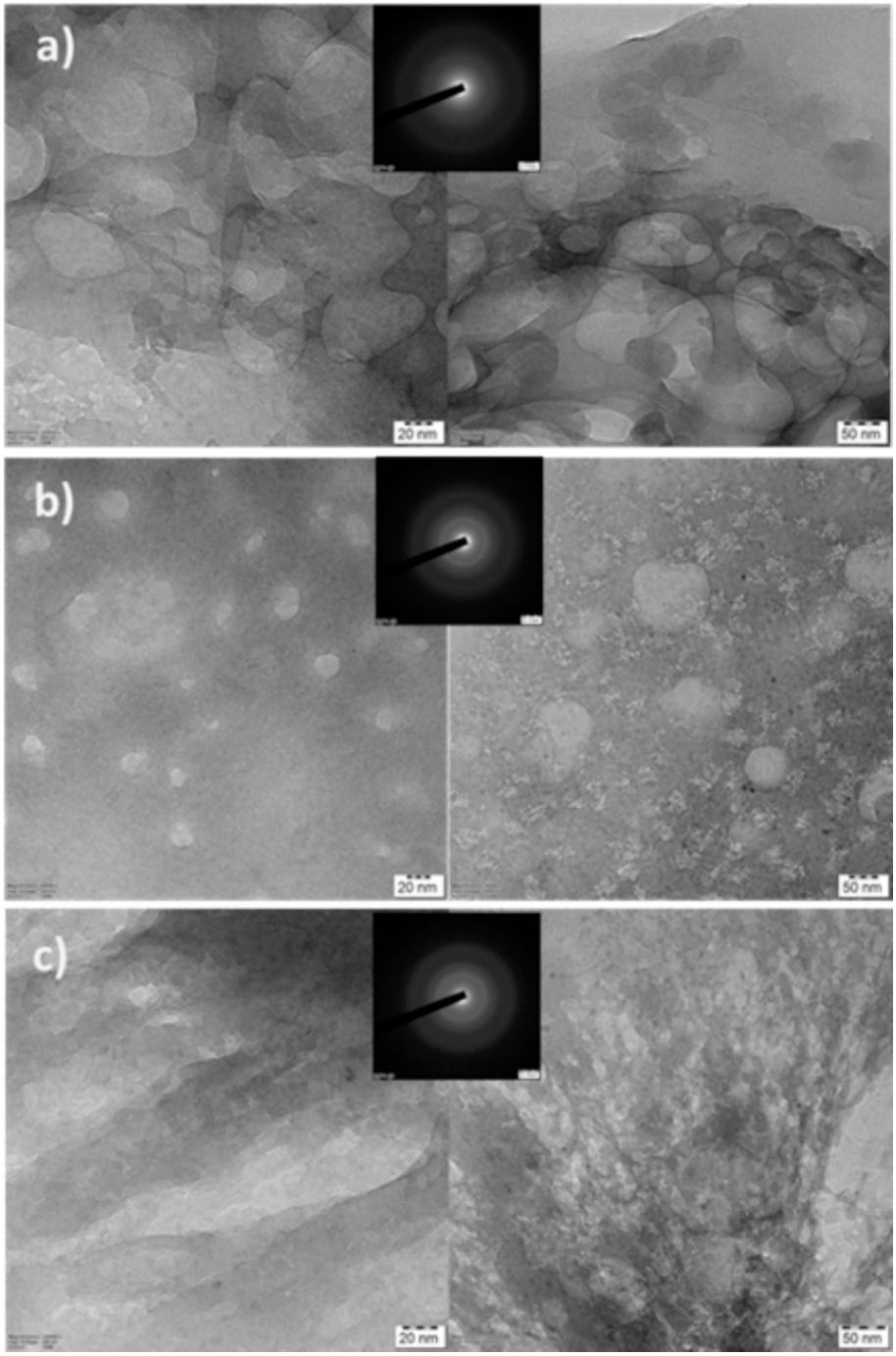


Fig. 4. TEM image of a) BNC hydrogel, b) G-GO5, and c) C-GO5 (inset – SAED).

(002) peak at 2θ equal to 25°, indicating the presence of the graphite crystallites [36]. The XRD pattern of BNC hydrogel displays a broad peak at 2θ equal to 20° corresponding to the (110) plane [50], indicating its amorphous nature [51]. The X-ray diffractograms of BNC/GO hydrogels (G-GO1, G-GO5, G-GO10, C-GO1, C-GO5, and C-GO10) do not exhibit any diffraction peaks similar to those of G-GO and C-GO. This result suggests high dispersion of GO in BNC/GO hydrogels because of the reaction between BNC molecules and GO in an aqueous solution, resulting in the disappearance of periodic interplanar spacing within GO sheets. Furthermore, the BNC/C-GO hydrogel peak shifts to a lower angle as compared to that in the BNC/G-GO hydrogel, implying an increase in interplanar distance due to the formation of face-to-edge assembly between BNC and C-GO.

3.2.1. *Porosity and swelling*

Due to the better performance in biological studies compared to higher concentration of fillers, G-GO5 and C-GO5 hydrogels were chosen for porosity, swelling and *in vitro* degradation studies. The swelling ratio was measured using PBS for the hydrogels. Swellings of G-GO5 and C-GO5 were in the range of 470% and 515% respectively (Fig. 8a). This was higher when compared to BNC hydrogel. When it comes to porosity studies compared to BNC hydrogel, porous nature of G-GO5 and C-GO5 was little higher (Fig. 8b). This increase in porosity and swelling ratio may be due to the presence of GO in the hydrogels.

3.2.2. *In vitro degradation*

Fig. 8c depicts the degradation assessed in PBS for all three samples

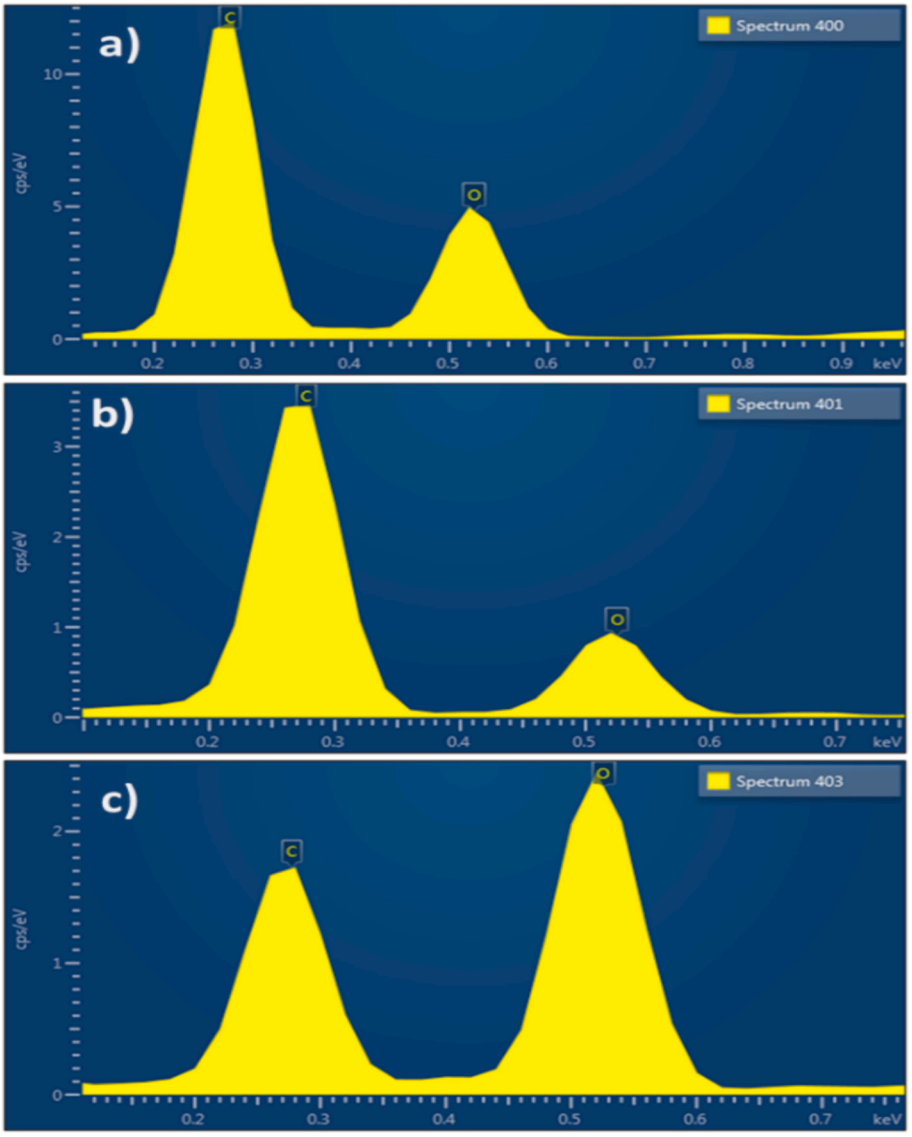


Fig. 5. EDAX of a) BNC hydrogel, b) G-GO5, and c) C-GO5.

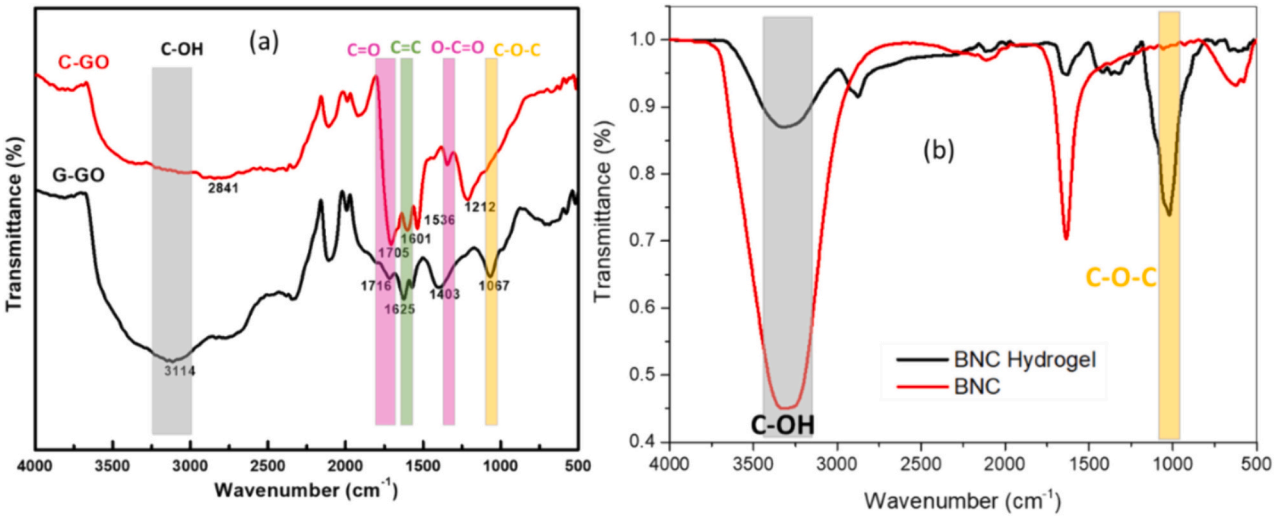
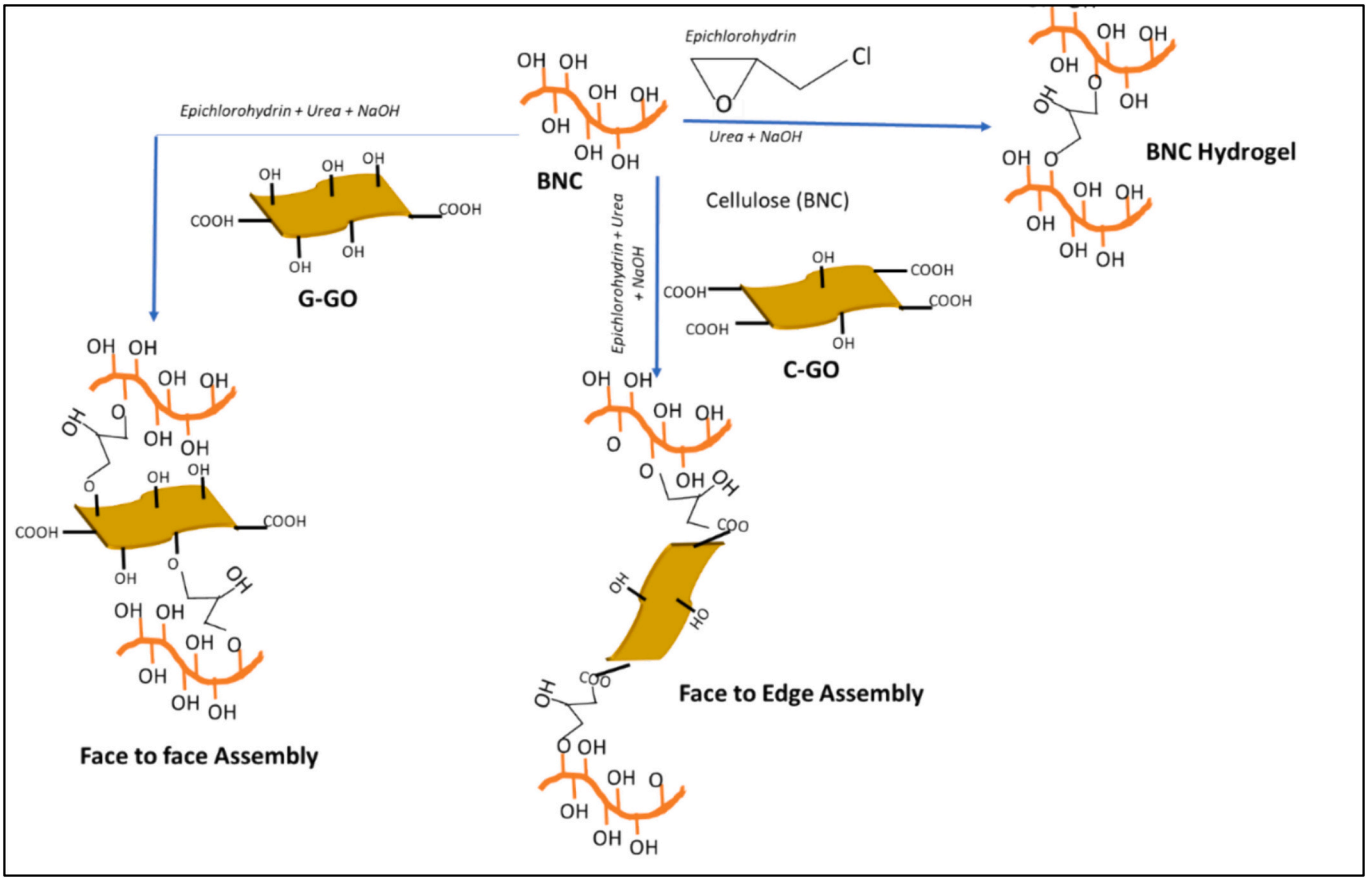


Fig. 6. FT-IR spectra of a) G-GO and C-GO, b) BNC and BNC hydrogel.



Scheme 1. Schematic of the mechanism of composite hydrogel formation with BNC by the face-to-face assembly and face-to-edge assembly of G-GO and C-GO, respectively.

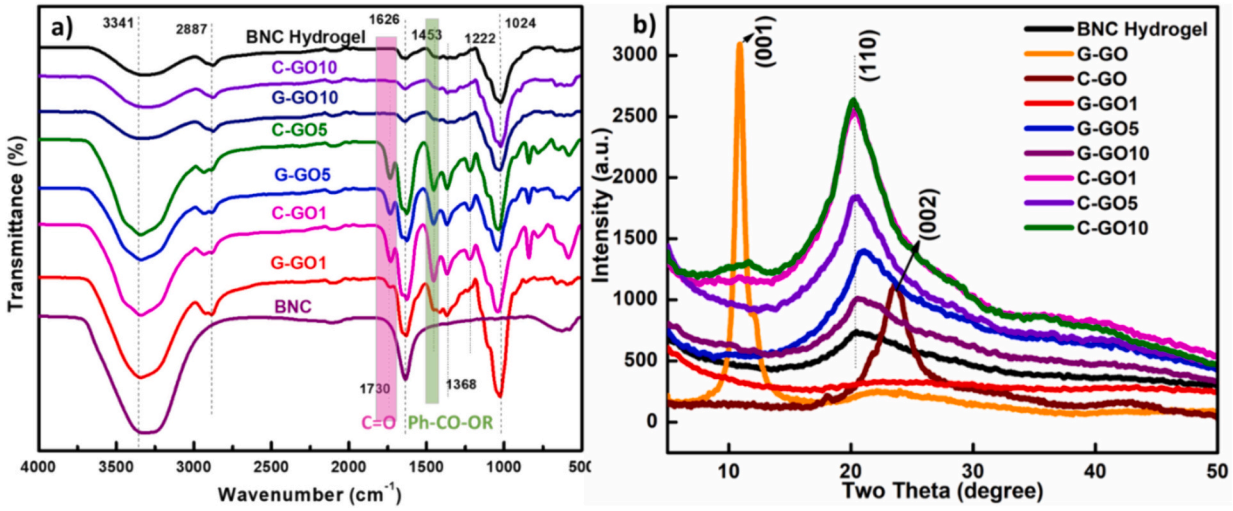


Fig. 7. a) FT-IR spectra of BNC, BNC/G-GO, and BNC/C-GO hydrogels. b) XRD patterns of G-GO, C-GO, BNC hydrogel, and BNC/GO hydrogels.

from Day 0 to Day 28 at 37°C. Even while there was no substantial weight loss after 7 days, the hydrogels began slowly deteriorating at the end of 28 days. This gradual degradation trend may be due to the presence of BNC and will be more beneficial for wound healing applications [52].

3.3. Thermal analysis

The thermal stability of the hydrogels was assessed by analyzing the TG-DTA plots. Fig. 9 and Table 2 illustrate the TG-DTA analysis of BNC hydrogel and BNC/GO hydrogels with varying concentrations of GO. All the hydrogel samples exhibited weight loss in three distinct stages. In the first stage, the temperature range was approximately 25°C to 249°C, accompanied by weight loss ranging from about 5% to 12%, primarily

Table 1
Functional groups present in BNC, G-GO, C-GO, and the hydrogels.

Functional groups	Wavenumbers cm^{-1}									
	BNC	G-GO	C-GO	BNC Hydrogel	G-GO1	G-GO5	G-GO10	C-GO1	C-GO5	C-GO10
O-H stretching	3296	3114	2841	3326	3340	3341	3341	3341	3340	3310
C-H stretching	–	–	–	2878	2880	2887	2878	2887	2869	2878
C=O stretch (acid)	–	1716	1702	–	–	–	–	–	–	–
C=O stretch (ester)	–	–	–	–	1736	1736	–	1736	1736	–
C=C stretching	1632	1625	1601	1632	1632	1626	1626	1632	1626	1626
Ph-CO-OR (ester)	–	–	–	–	–	1452	–	1455	1455	–
C-H stretching	–	–	–	–	1371	1371	–	1368	1371	–
C-O	–	–	–	–	–	1222	–	1222	1222	
C-O-C stretching	–	1067	–	1026	1026	1035	1024	1036	1024	1026

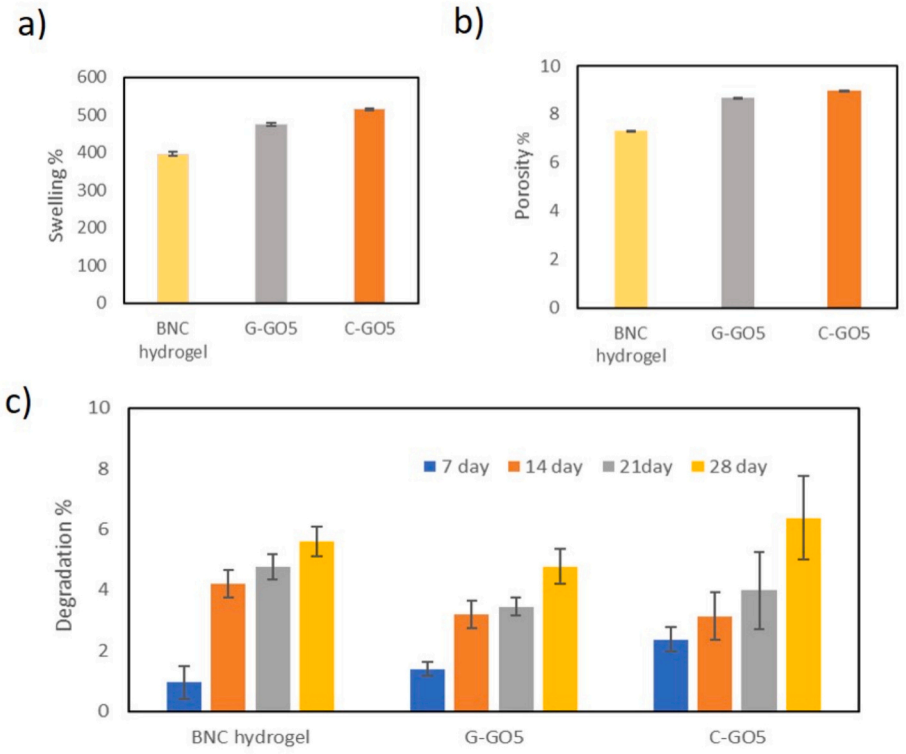


Fig. 8. a) Swelling – PBS absorption assay, b) Porosity – liquid displacement method, and c) *In vitro* degradation of the hydrogel immersed in PBS for 28 days.

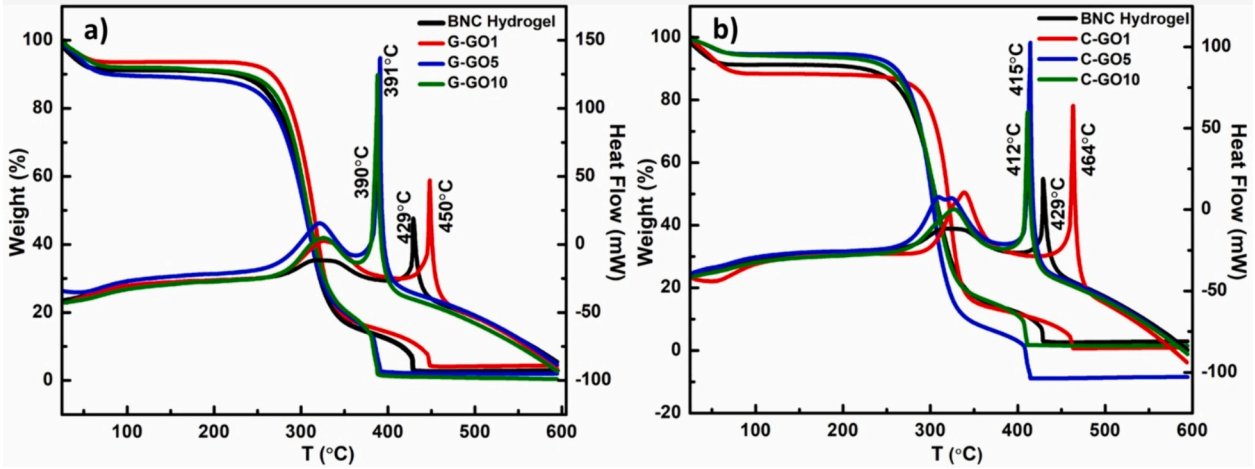


Fig. 9. TG-DTA curve of a) BNC/G-GO hydrogel and b) BNC/C-GO hydrogels.

Table 2
TG-DTA Analysis.

Samples	Weight loss (%)			Retention of weight % at 600 °C	1st Exothermic peak (°C)	2nd Exothermic peak (°C)
	1st stage (25–249) °C	2nd stage (202–433) °C	3rd stage (373–464) °C			
BNC Hydrogel	10	79	9	2	325	429
G-GO1	8	79	9	4	327	450
G-GO5	12	74	12	2	322	391
G-GO10	10	74	14	2	327	390
C-GO1	13	78	8	1	339	464
C-GO5	7	89	3	1	313	415
C-GO10	8	80	10	2	327	412

due to the evaporation of water absorbed by the hydrogel. The second stage, from 202°C to 433°C, was characterized by a weight loss of around 73% to 88%. Within this range, an exothermic peak was observed within the range of 313°C to 339°C which is due to the decomposition of functional groups present in the hydrogels. The third stage occurring between 373°C and 488°C, resulted in a weight loss of approximately 9% to 14%. This weight loss was attributed to the decomposition of carbon residues within the GO. Additionally, an exothermic peak appeared at 388°C to 464°C.

A closer examination of the data reveals that the BNC/GO hydrogels exhibit higher thermal stability up to 249°C compared to BNC hydrogel, which started to degrade at 202°C. Likewise, the C-GO hydrogels did not completely degrade until 464°C, while G-GO hydrogels completely degraded at 450°C.

3.4. Cytotoxicity analysis for hydrogel

As a potential candidate for wound healing applications, the toxicity of the BNC/GO hydrogels toward the surrounding cells in the wound environment was assessed. To this end, the viability of the L929 fibroblast cell line was calculated after 24 h culture in the presence of various hydrogel samples.

Fig. 10 presents the Alamar blue assay results for BNC hydrogel and different BNC/GO hydrogels: G-GO1, G-G05, G-G010, C-G01, C-G05, and C-G010 in L929 fibroblast cell lines. The cell viability was determined to be 96% for BNC hydrogel, 104% for BNC/G-GO1, 98% for BNC/G-GO5, 109% for BNC/G-GO10, 104% for BNC/C-GO1, 100% for BNC/C-GO5, and 89% for BNC/C-GO10. When Alamer blue values exceed 100%, it indicates cell growth in the hydrogel environment. According to ISO 10993-5:2009 guidelines, viability values >70% are considered non-toxic indicating that the hydrogels were not toxic to fibroblast cells. The BNC/GO hydrogels with various concentrations of G-GO and C-GO in the BNC hydrogel composite were evaluated, demonstrating low toxicity on the cell lines. Even at higher concentrations of GO incorporated into the hydrogel, the cell viability percentage remained above 80%. Moreover, there was no significant difference in cytotoxicity between G-GO and C-GO hydrogels. GO, owing to its abundant oxygen functional groups, promotes cell adherence and proliferation more effectively than graphene. Additionally, it has been observed that the cytotoxicity of GO depends on its concentration. Deepachitra et al. described that a low concentration of GO promotes better metabolic cell activity compared to that at high concentrations, as high concentrations diminish cell adhesion and increase cell apoptosis [53]. However, in this study, the overall results depict that GO up to 0.10 wt% concentration in BNC hydrogel had no toxic effects on cell biocompatibility. While performing cytotoxicity studies we noticed that morphology of cells was not altered after treating with hydrogel. In a nutshell, the cell viability study of BNC hydrogel and BNC/GO hydrogels demonstrates the biocompatibility of the hydrogels.

3.5. Antibacterial activity

The antibacterial properties of the prepared hydrogels in the presence of gram-negative *E. coli* bacteria from the Enterobacteriaceae family were investigated. This bacterium was selected since it is generally found in the guts, intestines, and in wound sites. The results reveal that of the two GOs, C-GO demonstrates superior antibacterial performance (Fig. 11).

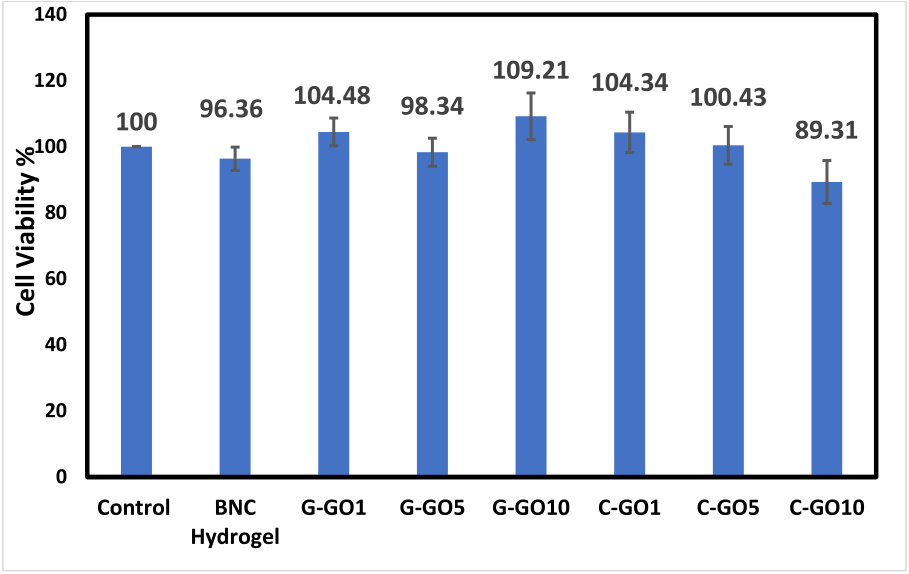


Fig. 10. Alamar blue assay of BNC hydrogel, and different BNC/GO hydrogels in L929 fibroblast cell lines.

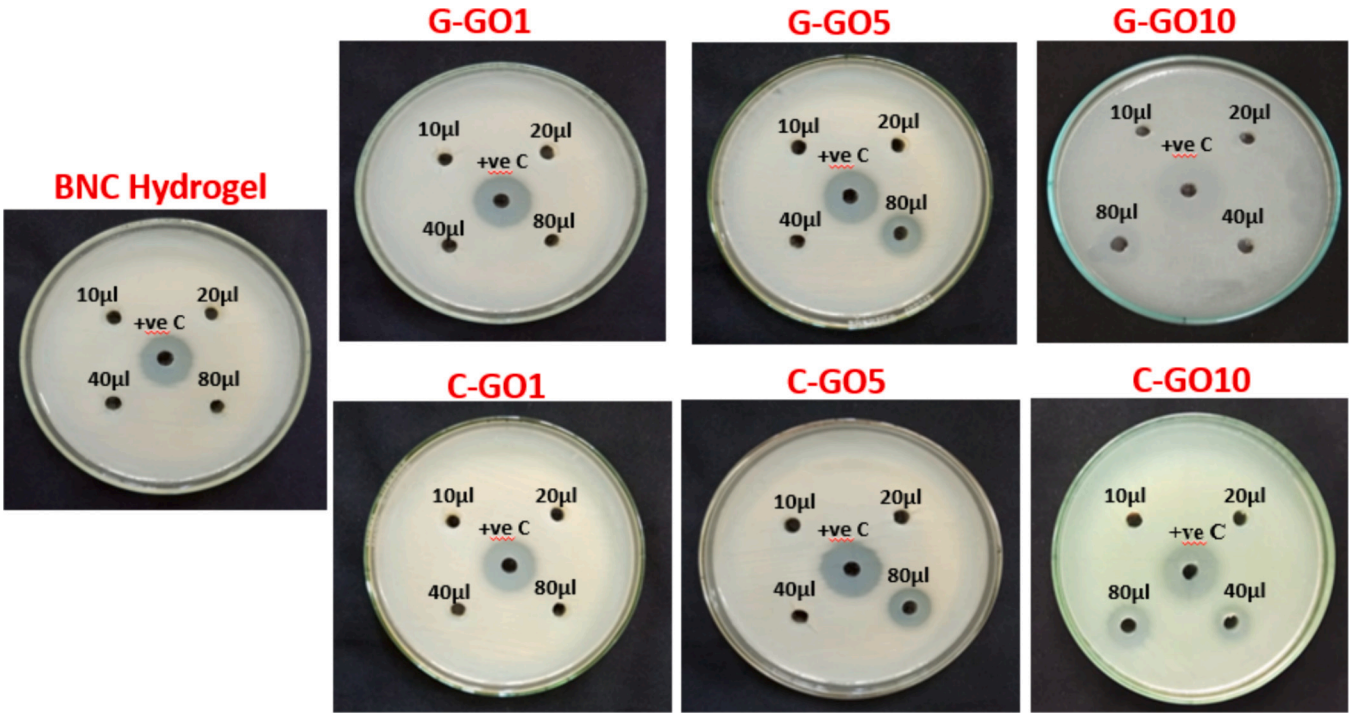


Fig. 11. Antibacterial activity of BNC Hydrogel and BNC/GO hydrogels in *E. coli*.

First, the extent of the ZOI is up to 17 mm for the C-GO compared to 15 mm for G-GO. Additionally, the Minimum Inhibitory Concentration (MIC) of C-GO is 40 µg/mL (ZOI-11 mm), whereas that of G-GO is 80 µg/mL (ZOI – 15 mm). This enhanced performance can be attributed to the face-to-edge assembly of the BNC/C-GO hydrogel, which allows uniform encapsulation and interconnection of GO, leading to better dispersion in the polymeric matrix.

In the basal-functionalized G-GO, specifically G-GO10, the ZOI decreased from 15 to 11 mm at the same level of inhibition concentration (80 µg/mL). This reduction is due to the agglomeration of G-GO at higher loading, as evidenced by the SEM images. On the other hand, for C-GO, even at the lower inhibition concentration (40 µg/mL), C-GO10 showed a ZOI of 11 mm. Furthermore, at the higher inhibition concentration of 80 µg/mL, the ZOI continued to increase with the increase in the loading of C-GO from 0.05 wt% to 0.10 wt%, albeit at a relatively small rate, suggesting that around this loading fraction, agglomeration may have started.

These findings align with our previous study [54] on the thermal performance of various carbonaceous materials, such as Multi-Walled Carbon Nanotubes (MWCNTs), Graphene Nanoplatelets (GNPs), Graphite-derived Multilayer Graphene (G-MLG), and Coal-derived Multilayer Graphene(C-MLG). There, the C-MLG outperformed all other carbonaceous thermally conductive materials when used as an additive in silicone thermal paste, primarily due to the presence of higher edge-oxygen functional groups in it. Also, we reported the optimum level of C-MLG loading fraction to be 3% compared to 2% in other carbonaceous additives. In the present work, a similar trend is observed in C-GO outperforming G-GO indicating that the loading fraction of C-GO reaches saturation at 0.10 wt%, while in G-GO, the saturation seems to reach at around a lower loading fraction of 0.05 wt% due to the earlier onset of agglomeration because of the larger lateral sizes of GO platelets in G-GO and the face-to-face crosslinking with the BNC network. The uniform size distribution of C-GO platelets and the face-to-edge crosslinking contribute to delaying the onset of agglomeration in C-GO, thereby increasing the ZOI.

Furthermore, in C-GO, the -COOH groups are used in networking with BNC, which leaves -OH groups free to bind with the cytoplasmic membrane and inhibit bacterial enzymes, thus augmenting the antibacterial activity through hydroxylation. In contrast, the -OH groups of G-GO are involved in networking, resulting in a lower availability of -OH groups for hydroxylation. Consequently, the affinity of G-GO with proteins is decreased, leading to a reduced ZOI [55].

3.6. *In vitro wound scratch assay*

As described in the experimental section, the wound-healing effectiveness of the BNC/GO hydrogels was assessed using an *in vitro* wound scratch assay. The scratch closure rate was measured at 24 h, 48 h, and 72 h intervals for the control BNC, G-GO5, and C-GO5 hydrogels. As illustrated in Fig. 12 the closure rate of C-GO5 is much better than G-GO5 from Day 1 onwards. The percentage rate of closure for G-GO5 is 47.3 ± 1, 67.2 ± 9, 82.6 ± 3 for 24 h,48 h, and 72 h respectively while for C-GO5 it is 66.3 ± 1, 78.2 ± 1, 90.4 ± 1 respectively.

These findings indicate that the C-GO5 hydrogels promote more efficient and noticeable wound mending, compared to the G-GO5. Thus, the results highlight the biocompatibility of BNC/C-GO hydrogels and their potential to facilitate cell migration, thereby promoting effective wound healing within a 3-day period.

4. Conclusion

The escalating prevalence of a wide range of acute injuries and chronic wounds worldwide poses a formidable challenge to current clinical therapeutics. Thus, the systematic management of wound infections and the selection of compatible active wound dressing materials are of paramount importance. This study centers on a comprehensive comparison of the physicochemical and active wound healing properties of two chemically distinct GOs derived from two different sources-graphite and coal. The unique structures of these GOs, namely — edge-functionalized C-GO and basal functionalized G-GO when incorporated into BNC reveal diverse characteristics, shedding light on their physicochemical and active wound healing properties. The results reveal that BNC/C-GO shows superior physicochemical and wound-healing properties compared to BNC/G-GO. The presence of GO increases the

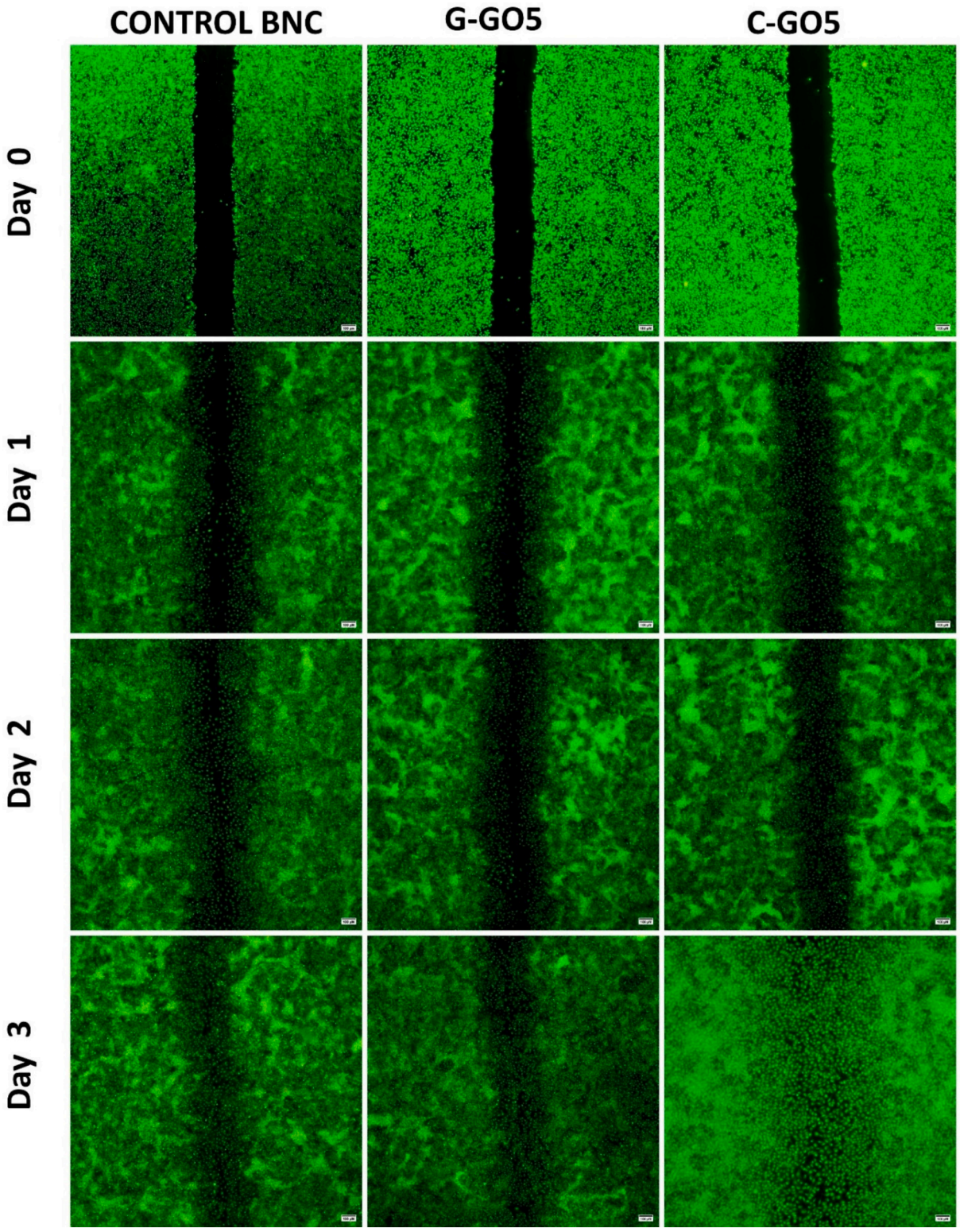


Fig. 12. *In vitro* wound scratch assay of BNC/GO hydrogels. Scale bar = 100 μm.

porosity and swelling ratio of BNC/GO hydrogels. BNC/C-GO hydrogels demonstrate higher thermal stability and C-GO5 shows the best antibacterial properties while maintaining biocompatibility. The scratch assay indicates that BNC/C-GO hydrogel exhibits a superior wound healing rate. Hence, 0.05 wt% C-GO incorporated BNC is the optimal composite for active wound healing.

These findings address the need for low-cost, environmentally friendly, and biocompatible active advanced wound dressing materials. The C-GO encapsulated BNC hydrogel emerges as a promising and versatile material for the development of a sustainable active wound dressing in biomedical applications. It is essential to note that this study is confined to the evaluation of physicochemical properties and *in vitro* studies of hydrogel. Future pre-clinical studies are planned to focus on investigating BNC/C-GO hydrogels as efficient wound-dressing agents in

clinical applications.

Ethics approval and consent to participate

Not Applicable.

Funding

Not applicable.

CRediT authorship contribution statement

Chithra Lekha P: Writing – review & editing, Writing – original draft, Visualization, Validation, Project administration, Methodology, Investigation, Formal analysis, Data curation, Conceptualization. **Marini L:** Writing – review & editing, Formal analysis, Data curation. **Suman K. Jhajharia:** Writing – review & editing, Formal analysis, Conceptualization. **Aadinath W:** Writing – review & editing, Formal analysis, Data curation. **Vignesh Muthuvijayan:** Writing – review & editing, Supervision, Resources, Formal analysis, Data curation. **Mareeswari Paramasivan:** Writing – review & editing, Formal analysis, Data curation. **Monica Chingchuilin Gonmei:** Writing – review & editing, Formal analysis, Data curation. **M.K. Padmanabhan:** Writing – review & editing, Supervision, Resources, Project administration, Funding acquisition. **Madhan Jeyaraman:** Writing – review & editing, Validation, Conceptualization. **Roop L. Mahajan:** Writing – review & editing, Visualization, Validation, Supervision, Resources, Project administration, Conceptualization.

Declaration of competing interest

The authors declare that they have no known competing financial interests or personal relationships that could have appeared to influence the work reported in this paper.

Availability of data and materials

All data generated or analyzed during this study are included in this published article.

Acknowledgments

Not applicable

Appendix A. Supplementary data

Supplementary data to this article can be found online at https://doi.org/10.1016/j.ijbiomac.2024.132589.

References

[1] R. Li, K. Liu, X. Huang, D. Li, J. Ding, B. Liu, X. Chen, Bioactive materials promote wound healing through modulation of cell behaviors, Adv. Sci. 9 (2022), https://doi.org/10.1002/advs.202105152.
[2] R. Yu, H. Zhang, B. Guo, Conductive biomaterials as bioactive wound dressing for wound healing and skin tissue engineering, Nano Lett. 14 (2022), https://doi.org/10.1007/s40820-021-00751-y.
[3] T. Li, M. Sun, S. Wu, State-of-the-art review of electrospun gelatin-based nanofiber dressings for wound healing applications, Nanomaterials 12 (2022) 784, https://doi.org/10.3390/nano12050784.
[4] A.J. Singer, R.A.F. Clark, Cutaneous wound healing, Doi:10.1056/NEJM199909023411006 341 (1999) 738–746, https://doi.org/10.1056/NEJM199909023411006.
[5] H. Wang, Z. Xu, M. Zhao, G. Liu, J. Wu, Advances of hydrogel dressings in diabetic wounds, Biomater. Sci. 9 (2021) 1530–1546, https://doi.org/10.1039/d0bm01747g.
[6] H.R. Moreira, A.P. Marques, Vascularization in skin wound healing: where do we stand and where do we go? Curr. Opin. Biotechnol. 73 (2022) 253–262, https://doi.org/10.1016/j.copbio.2021.08.019.
[7] A. Kushwaha, L. Goswami, B.S. Kim, Nanomaterial-based therapy for wound healing, Nanomaterials 12 (2022), https://doi.org/10.3390/nano12040618.
[8] H. Moradpoor, H. Mohammadi, M. Safaei, H.R. Mozaffari, R. Sharifi, P. Gorji, A. B. Sulong, N. Muhamad, M. Ebadi, Recent advances on bacterial cellulose-based wound management: promises and challenges, Int. J. Polym. Sci. 2022 (2022), https://doi.org/10.1155/2022/1214734.
[9] Z. Fan, B. Liu, J. Wang, S. Zhang, Q. Lin, P. Gong, L. Ma, S. Yang, A novel wound dressing based on ag/graphene polymer hydrogel: effectively kill bacteria and accelerate wound healing, Adv. Funct. Mater. 24 (2014) 3933–3943, https://doi.org/10.1002/adfm.201304202.
[10] S. Alven, B.A. Aderibigbe, Chitosan and cellulose-based hydrogels for wound management, Int. J. Mol. Sci. 21 (2020) 1–30, https://doi.org/10.3390/ijms21249656.
[11] W.C. Lin, C.C. Lien, H.J. Yeh, C.M. Yu, S.H. Hsu, Bacterial cellulose and bacterial cellulose-chitosan membranes for wound dressing applications, Carbohydr. Polym. 94 (2013) 603–611, https://doi.org/10.1016/j.carbpol.2013.01.076.
[12] J. Ahmed, M. Gultekinoglu, M. Edirisinghe, Bacterial cellulose micro-nano fibres for wound healing applications, Biotechnol. Adv. 41 (2020), https://doi.org/10.1016/j.biotechadv.2020.107549.
[13] L. Fu, P. Zhou, S. Zhang, G. Yang, Evaluation of bacterial nanocellulose-based uniform wound dressing for large area skin transplantation, Mater. Sci. Eng. C 33 (2013) 2995–3000, https://doi.org/10.1016/j.msec.2013.03.026.
[14] M.W. Ullah, S. Manan, S.J. Kiprono, M. Ul-Islam, G. Yang, Synthesis, structure, and properties of bacterial cellulose, in: Nanocellulose: From Fundamentals to Advanced Materials, Wiley, 2019, pp. 81–114, https://doi.org/10.1002/9783527807437.ch4.
[15] T.V. Patil, D.K. Patel, S.D. Dutta, K. Ganguly, K.T. Lim, Graphene oxide-based stimuli-responsive platforms for biomedical applications, Molecules 26 (2021), https://doi.org/10.3390/molecules26092797.
[16] P. Zare, M. Aleemardani, A. Seifalian, Z. Bagher, A.M. Seifalian, Graphene oxide: opportunities and challenges in biomedicine, Nanomaterials (Basel). 11 (5) (2021 Apr 22) 1083, https://doi.org/10.3390/nano11051083.
[17] G. Liao, J. Hu, Z. Chen, R. Zhang, G. Wang, T. Kuang, Preparation, properties, and applications of graphene-based hydrogels, Front. Chem. (6) (2018 Oct 1) 450, https://doi.org/10.3389/fchem.2018.00450.
[18] A.A. Ghawanmeh, G.A.M. Ali, H. Algarni, S.M. Sarkar, K.F. Chong, Graphene oxide-based hydrogels as a nanocarrier for anticancer drug delivery, Nano Res. 12 (2019) 973–990, https://doi.org/10.1007/s12274-019-2300-4.
[19] M. Soliman, A.A. Sadek, H.N. Abdelhamid, K. Hussein, Graphene oxide-cellulose nanocomposite accelerates skin wound healing, Res. Vet. Sci. 137 (2021) 262–273, https://doi.org/10.1016/j.rvsc.2021.05.013.
[20] Y. Liu, J. Ding, Q.Q. Wang, M.L. Wen, T.T. Tang, Y. Liu, R. Yuan, Y.F. Li, M.W. An, Research progress on the biomedical uses of graphene and its derivatives, Xinxing Tan Cailiao/New Carbon Mater. 36 (2021) 779–793, https://doi.org/10.1016/S1872-5805(21)60073-2.
[21] Y. Liang, B. Chen, M. Li, J. He, Z. Yin, B. Guo, Injectable antimicrobial conductive hydrogels for wound disinfection and infectious wound healing, Biomacromolecules 21 (2020) 1841–1852, https://doi.org/10.1021/acs.biomac.9b01732.
[22] A. Pourjavadi, Z. Mazaheri Tehrani, H. Salami, F. Seidi, A. Motamedi, A. Amanzadi, E. Zayerzadeh, M. Shabanian, Both tough and soft double network hydrogel nanocomposite based on O-carboxymethyl chitosan/poly(vinyl alcohol) and graphene oxide: a promising alternative for tissue engineering, Polym. Eng. Sci. 60 (2020) 889–899, https://doi.org/10.1002/pen.25297.
[23] A. Sadeghianmaryan, Y. Karimi, S. Naghieh, H. Alizadeh Sardroud, M. Gorji, X. Chen, Electrospinning of scaffolds from the Polycaprolactone/polyurethane composite with graphene oxide for skin tissue engineering, Appl. Biochem. Biotechnol. 191 (2020) 567–578, https://doi.org/10.1007/s12010-019-03192-x.
[24] M. di Luca, O. Vittorio, G. Cirillo, M. Curcio, M. Czuban, F. Voli, A. Farfalla, S. Hampel, F.P. Nicoletta, F. Iemma, Electro-responsive graphene oxide hydrogels for skin bandages: the outcome of gelatin and trypsin immobilization, Int. J. Pharm. 546 (2018) 50–60, https://doi.org/10.1016/j.ijpharm.2018.05.027.
[25] Q. Zhang, Q. Du, Y. Zhao, F. Chen, Z. Wang, Y. Zhang, H. Ni, H. Deng, Y. Li, Y. Chen, Graphene oxide-modified electrospun polyvinyl alcohol nanofibrous scaffolds with potential as skin wound dressings, RSC Adv. 7 (2017) 28826–28836, https://doi.org/10.1039/c7ra03997b.
[26] P. Yu, R.Y. Bao, X.J. Shi, W. Yang, M.B. Yang, Self-assembled high-strength hydroxyapatite/graphene oxide/chitosan composite hydrogel for bone tissue engineering, Carbohydr. Polym. 155 (2017) 507–515, https://doi.org/10.1016/j.carbpol.2016.09.001.
[27] A. Azarniya, N. Eslahi, N. Mahmoudi, A. Simchi, Effect of graphene oxide nanosheets on the physico-mechanical properties of chitosan/bacterial cellulose nanofibrous composites, Compos. Part A Appl. Sci. Manuf. 85 (2016) 113–122, https://doi.org/10.1016/j.compositesa.2016.03.011.
[28] X. Rui-Hong, R. Peng-Gang, H. Jian, R. Fang, R. Lian-Zhen, S. Zhen-Feng, Preparation and properties of graphene oxide-regenerated cellulose/polyvinyl alcohol hydrogel with pH-sensitive behavior, Carbohydr. Polym. 138 (2016) 222–228, https://doi.org/10.1016/j.carbpol.2015.11.042.
[29] Y. Liu, M. Park, H.K. Shin, B. Pant, J. Choi, Y.W. Park, J.Y. Lee, S.J. Park, H.Y. Kim, Facile preparation and characterization of poly(vinyl alcohol)/chitosan/graphene oxide biocomposite nanofibers, J. Ind. Eng. Chem. 20 (2014) 4415–4420, https://doi.org/10.1016/j.jiec.2014.02.009.
[30] Z. Fan, B. Liu, J. Wang, S. Zhang, Q. Lin, P. Gong, L. Ma, S. Yang, A novel wound dressing based on ag/graphene polymer hydrogel: effectively kill bacteria and accelerate wound healing, Adv. Funct. Mater. 24 (2014) 3933–3943, https://doi.org/10.1002/adfm.201304202.

[31] M.F.P. Graça, B.L. Melo, R. Lima-Sousa, P. Ferreira, A.F. Moreira, I.J. Correia, Reduced graphene oxide-enriched chitosan hydrogel/cellulose acetate-based nanofibers application in mild hyperthermia and skin regeneration, Int. J. Biol. Macromol. 229 (2023) 224–235, https://doi.org/10.1016/j.ijbiomac.2022.12.291.
[32] D.R. Ningrum, W. Hanif, D.F. Mardhian, L.A.T.W. Asri, In vitro biocompatibility of hydrogel polyvinyl alcohol/Moringa oleifera leaf extract/graphene oxide for wound dressing, Polymers (Basel) 15 (2023), https://doi.org/10.3390/polym15020468.
[33] M.U.A. Khan, G.M. Stojanović, R. Hassan, T.J.S. Anand, M. Al-Ejji, A. Hasan, Role of graphene oxide in bacterial cellulose−gelatin hydrogels for wound dressing applications, ACS Omega 8 (2023) 15909–15919, https://doi.org/10.1021/acsomega.2c07279.
[34] X. Ou, L. Guan, W. Guo, X. Zhang, S. Wu, D. Guo, R. Li, A.V. Zvyagin, Q. Lin, W. Qu, Graphene oxide-based injectable conductive hydrogel dressing with immunomodulatory for chronic infected diabetic wounds, Mater. Des. 224 (2022), https://doi.org/10.1016/j.matdes.2022.111284.
[35] M.U.A. Khan, S.I.A. Razak, A. Hassan, S. Qureshi, G.M. Stojanović, Ihsan-Ul-Haq, multifunctional Arabinoxylan-functionalized-graphene oxide based composite hydrogel for skin tissue engineering, Front. Bioeng. Biotechnol. 10 (2022), https://doi.org/10.3389/fbioe.2022.865059.
[36] S.Y. Lee, R.L. Mahajan, A facile method for coal to graphene oxide and its application to a biosensor, Carbon N Y 181 (2021) 408–420, https://doi.org/10.1016/j.carbon.2021.05.007.
[37] V.C. Hoang, M. Hassan, V.G. Gomes, Coal derived carbon nanomaterials – recent advances in synthesis and applications, Appl. Mater. Today 12 (2018) 342–358, https://doi.org/10.1016/j.apmt.2018.06.007.
[38] D. Jankus, Antimicrobial Properties of Graphite and Coal-Derived Graphene Oxides as an Advanced Coating for Titanium Implants, 2021.
[39] J.L. Suter, P.V. Coveney, Principles governing control of aggregation and dispersion of aqueous graphene oxide, Sci. Rep. 11 (2021), https://doi.org/10.1038/s41598-021-01626-3.
[40] R. Jayabalan, R.V. Malbaša, E.S. Lončar, J.S. Vitas, M. Sathishkumar, A review on kombucha tea-microbiology, composition, fermentation, beneficial effects, toxicity, and tea fungus, Compr. Rev. Food Sci. Food Saf. 13 (2014) 538–550, https://doi.org/10.1111/1541-4337.12073.
[41] S.K. Jhajharia, K. Selvaraj, Non-templated ambient nanoperforation of graphene: a novel scalable process and its exploitation for energy and environmental applications, Nanoscale 7 (2015) 19705–19713, https://doi.org/10.1039/c5nr05715a.
[42] H. Kanniyappan, P. Thangavel, S. Chakraborty, V. Arige, V. Muthuvijayan, Design and evaluation of Konjac glucomannan-based bioactive interpenetrating network (IPN) scaffolds for engineering vascularized bone tissues, Int. J. Biol. Macromol. 143 (2020) 30–40, https://doi.org/10.1016/j.ijbiomac.2019.12.012.
[43] G. Perumal, S. Pappuru, D. Chakraborty, A. Maya Nandkumar, D.K. Chand, M. Doble, Synthesis and characterization of curcumin loaded PLA—Hyperbranched polyglycerol electrospun blend for wound dressing applications, Mater. Sci. Eng. C 76 (2017) 1196–1204, https://doi.org/10.1016/j.msec.2017.03.200.
[44] C.C. Liang, A.Y. Park, J.L. Guan, In vitro scratch assay: a convenient and inexpensive method for analysis of cell migration in vitro, Nat. Protoc. 2 (2007) 329–333, https://doi.org/10.1038/nprot.2007.30.
[45] A. Barroso, H. Mestre, A. Ascenso, S. Simões, C. Reis, Nanomaterials in wound healing: from material sciences to wound healing applications, Nano Select 1 (2020) 443–460, https://doi.org/10.1002/nano.202000055.
[46] M. Kithiyon, B. Pannerselvam, S. Sharma Balasaubramaniyam Madhukumar, J. Sridharan, T.S. Alagumuthu, Efficacy of mycosynthesised AgNPs from Earliella scabrosa as an in vitro antibacterial and wound healing agent, IET Nanobiotechnol. 13 (2019) 339–344, https://doi.org/10.1049/iet-nbt.2018.5237.
[47] M.K. Rabchinskii, S.D. Saveliev, S.A. Ryzhkov, E.K. Nepomnyashchaya, S.I. Pavlov, M.V. Baidakova, P.N. Brunkov, Establishing the applicability of the laser diffraction technique for the graphene oxide platelets lateral size measurements, in: J Phys Conf Ser, IOP Publishing Ltd, 2020, https://doi.org/10.1088/1742-6596/1695/1/012070.
[48] X. Liu, T. Zhang, K. Pang, Y. Duan, J. Zhang, Graphene oxide/cellulose composite films with enhanced UV-shielding and mechanical properties prepared in NaOH/urea aqueous solution, RSC Adv. 6 (2016) 73358–73364, https://doi.org/10.1039/c6ra16535d.
[49] F.T. Johra, J.W. Lee, W.G. Jung, Facile and safe graphene preparation on solution based platform, J. Ind. Eng. Chem. 20 (2014) 2883–2887, https://doi.org/10.1016/j.jiec.2013.11.022.
[50] X. Chen, S. Zhou, L. Zhang, T. You, F. Xu, Adsorption of heavy metals by graphene oxide/cellulose hydrogel prepared from NaOH/urea aqueous solution, Materials 9 (2016), https://doi.org/10.3390/MA9070582.
[51] F. Wahid, H. Bai, F.P. Wang, Y.Y. Xie, Y.W. Zhang, L.Q. Chu, S.R. Jia, C. Zhong, Facile synthesis of bacterial cellulose and polyethyleneimine based hybrid hydrogels for antibacterial applications, Cellulose 27 (2020) 369–383, https://doi.org/10.1007/S10570-019-02806-1/METRICS.
[52] S. Ullah, X. Chen, Fabrication, applications and challenges of natural biomaterials in tissue engineering, Appl. Mater. Today 20 (2020) 100656, https://doi.org/10.1016/j.apmt.2020.100656.
[53] R. Deepachitra, V. Ramnath, T.P. Sastry, Graphene oxide incorporated collagen-fibrin biofilm as a wound dressing material, RSC Adv. 4 (2014) 62717–62727, https://doi.org/10.1039/c4ra10150b.
[54] Bharadwaj, B.; Singh, P.; Mahajan, R.L. Thermal performance of different carbonaceous nanoparticles as additives to thermal paste as an interface material. *Proceedings of ASME 2021 International Technical Conference and Exhibition on Packaging and Integration of Electronic and Photonic Microsystems, InterPACK* **2021**, doi:https://doi.org/10.1115/IPACK2021-69254.
[55] M. Miklasińska-Majdanik, M. Kępa, R.D. Wojtyczka, D. Idzik, T.J. Wąsik, Phenolic compounds diminish antibiotic resistance of staphylococcus aureus clinical strains, Int. J. Environ. Res. Public Health 15 (2018), https://doi.org/10.3390/ijerph15102321.